An Idealized 1½-Layer Isentropic Model with Convection and Precipitation for Satellite Data Assimilation Research. Part I: Model Dynamics

LUCA CANTARELLO,[a] ONNO BOKHOVE,[a] AND STEVEN TOBIAS[a]

[a] School of Mathematics, University of Leeds, Leeds, United Kingdom

ABSTRACT: An isentropic 1½-layer model based on modified shallow-water equations is presented, including terms mimicking convection and precipitation. This model is an updated version of the isopycnal single-layer modified rotating shallow water (modRSW) model. The clearer link between fluid temperature and model variables together with a double-layer structure make this revised, isentropic model a more suitable tool to achieve our future goal: to conduct idealized experiments for investigating satellite data assimilation. The numerical model implementation is verified against an analytical solution for stationary waves in a rotating fluid, based on Shrira's methodology for the isopycnal case. Recovery of the equivalent isopycnal model is also verified, both analytically and numerically. With convection and precipitation added, we show how complex model dynamics can be achieved exploiting rotation and relaxation to a meridional jet in a periodic domain. This solution represents a useful reference simulation or "truth" in conducting future (satellite) data assimilation experiments, with additional atmospheric conditions and data. A formal analytical derivation of the isentropic 1½-layer model from an isentropic two-layer model without convection and precipitation is shown in a companion paper (Part II).

KEYWORDS: Data assimilation; Nonlinear models; Primitive equations model; Idealized models; Shallow-water equations

1. Introduction

Satellites are one of the main sources of observations in atmospheric data assimilation (DA). Since they became part of the Global Observing System (GOS) in 1979, they have greatly improved the quality of weather forecasting, especially in the Southern Hemisphere (Simmons and Hollingsworth 2002; Rabier 2005).

The preeminent position of satellite observations in most weather forecasting systems continues the need for research on how to expand their use in a more efficient and impactful way. Recently, for example, more resources have been directed toward the assimilation of all-sky observations (Geer et al. 2017, 2018; Migliorini and Candy 2019). However, because of the high computational resources required to run an operational DA scheme and the huge amount of satellite data available today, research in satellite DA using operational schemes can be a challenging task. Unsurprisingly, the development and the use of a wide range of simpler models has been explored in recent years to support DA research (Ehrendorfer and Errico 2008; Vetra-Carvalho et al. 2011; Rudd et al. 2012; Stewart et al. 2013; Würsch and Craig 2014, hereafter W&C; Smith et al. 2015; Petrie et al. 2017; Zaplotnik et al. 2018; Bannister 2020). The use of rotating shallow-water models to investigate various topics in atmospheric sciences and oceanography constitutes a well-known possibility, as discussed at length in Zeitlin (2018). In particular, isentropic, multilayer shallow-water models with moisture and precipitation represent a powerful tool to investigate a number of dynamic meteorology features (Rostami and Zeitlin 2020,

2021, 2022). In this paper, we propose a similar model for satellite DA research.

Previous research had led to the development of an isopycnal, idealized model for convection and precipitation, henceforth called "modRSW," based on augmented shallow-water equations (Kent et al. 2017; Kent 2016), which extended and improved the shallow-water model developed by W&C. The W&C model imitates cumulus convection and precipitation through a system of switches based on fluid depth thresholds and avoids the explicit modeling of moisture (Q) and precipitation (P) through a Q/P equation, which is typical of other "moist" isentropic shallow-water models, such as those presented Bouchut et al. (2009) and Lambaerts et al. (2011). Moreover, the use of switches to alter the dynamics of the system is an important feature commonly found in state-of-the-art NWP models, which enhances nonlinearity. Despite its simplicity, the W&C model has proven to be a valuable tool to investigate various aspects of convective-scale DA, such as the use of particle filters (Haslehner et al. 2016), the parameter estimation for the representation of clouds (Ruckstuhl and Janjić 2018), and the representation of model error (Zeng et al. 2018, 2019). As discussed in Kent et al. (2017), the modRSW model combines the simple configuration of W&C with important adjustments to the model equations such that the system can include rotation and becomes hyperbolic. The latter aspect facilitates its robust numerical implementation. Last, the ability of the modRSW model to continuously generate and remove rain from the system offers a convenient alternative to the explicit modeling of vaporization.

In later work, the modRSW model was used to conduct idealized forecast-assimilation experiments proving its suitability and relevance for numerical weather prediction (NWP) data assimilation research (Kent et al. 2020). Further work concerns the inclusion of idealized satellite data assimilation

simulations (Cantarello 2021). Unfortunately, limitations for modRSW's use in satellite DA have emerged and an extension of the model is necessary. Hence, in this paper, modifications to the model are undertaken in order to make it suitable for satellite DA research.

One of the most impactful types of satellite data used in operational NWP systems are passive observations[1] of emitted thermal radiation coming from Earth's surface and atmosphere. This radiation can be related to the temperature of the emitting source (and vice versa) by exploiting the principles of radiative transfer and blackbody radiation. Therefore, in order to perform sensible satellite DA in an idealized fashion, it is essential that either (i) the background model includes temperature among the prognostic variables or (ii) one (or more) of the model variables can be readily related to temperature.

Regarding the latter issue, the modRSW model is not particularly well suited, since it does not include temperature among its prognostic variables, and even though a simple diagnostic relationship between fluid depth and temperature can be formulated (based on the hydrostatic equilibrium and the ideal gas law), this leads to some scaling issues in which DA-relevant model dynamics can be achieved only for unrealistic values of the temperature. A second big limitation posed by the modRSW model is the fact that it is based on a single layer of fluid, which hampers the possibility of working with vertically complex observations, an essential feature that needs to be replicated in the context of satellite DA.

Given the above issues, we have formulated the following modifications of the modRSW model:

1) we use a 1½-layer model instead of a single-layer model, adding a passive layer on top, nearly at rest, and effectively capped by a rigid lid; and

2) we replaced the isopycnal model, with its uniform layer density, by an isentropic model, in which the potential temperature (or the entropy) is constant within each layer.

Although the first modification would require only the replacement of the acceleration due to gravity with a so-called reduced gravity g', the second leads to a somewhat different set of equations. Previous work done by Bokhove and Oliver (2009) has shown that, starting from the (hydrostatic) primitive equations, a multilayer shallow-water model can be derived using Hamiltonian fluid dynamics. In a separate companion paper (Bokhove et al. 2022, hereafter Part II) we will show a fully consistent mathematical derivation of a "dry" isentropic 1½-layer shallow-layer model (i.e., without convection and precipitation) which originates from that work. In addition, we will use that paper to discuss the physical scaling utilized in this study, proving that can be justified on the basis of real-world observations.

The newly derived "moist" model, denoted by "ismodRSW," retains the system of switches to mimic convection and precipitation already used in the modRSW model, as well as all the improvements over the W&C model discussed above. At the same time, it also incorporates a much more robust definition of temperature for each layer, since the temperature T for an isentropic fluid is linked to the definition of its potential temperature θ:

$$\theta = T\left(\frac{p_r}{p}\right)^{\kappa} \Rightarrow T = \theta\left(\frac{p}{p_r}\right)^{\kappa} = \theta\eta^{\kappa}, \tag{1}$$

in which p is the pressure, p_r a reference pressure, and $\kappa = R/C_p$ the ratio between the specific gas constant for dry air ($R = 287$ J kg^{-1} K^{-1}) and its specific heat capacity at constant pressure ($c_p = 1004$ J kg^{-1} K^{-1}), with $\eta = p/p_r$ a key variable in the isentropic model's lower layer; $\Pi = \eta^{\kappa}$ is also referred in the literature as the *Exner function*.

Given the physically consistent definition in (1), the isentropic configuration contributes to solve the scaling issues arising in the modRSW model once equipped with a simpler relationship between temperature and fluid depth (cf. section 2a). The advantage of using an isentropic model is apparent in a paper by Pan and Smith (1999), where the isentropic reduced gravity is used to estimate g' from the observations in their classic (isopycnal) reduced-gravity shallow-water model. Additionally, the presence of the second, upper layer will help to increase the vertical complexity with which we describe the atmosphere yielding a more realistic testbed for satellite DA.

Last, we note that the presence of bottom topography has not be considered in this study.

The structure of the paper is as follows. In section 2 the benefits brought about by the new setup are highlighted, the "dry" 1½-layer model (i.e., without convection and precipitation) is presented and subsequently put into conservative hyperbolic form. In section 3, the comparison of robust numerics with an adapted analytical solution originally proposed by Shrira for nonlinear isopycnal shallow-water waves is shown as a numerical verification step, cf. Shrira (1981, 1986). In section 4, the "moist" isentropic model endowed with convection and precipitation is outlined and a prototype of numerical simulation to be used in future forecast-assimilation experiments is discussed. Conclusions are provided in section 5.

2. An isentropic 1½-layer shallow-water model

a. Motivation

The development of a new, isentropic 1½-layer shallow-water model is motivated by the limitations posed by the single-layer modRSW model developed by Kent et al. (2017) in conducting idealized satellite data assimilation experiments. In this regard, the main issues are the lack of a robust physical definition of fluid temperature and the unrealistic scaling.

One way to proceed would be to equip the modRSW model with a simple diagnostic equation between the dimensionless

---

[1] In satellite meteorology, "passive" observations are measurements of radiation emitted by Earth's surface and atmosphere or emitted by the sun and subsequently reflected toward the satellite.

TABLE 1. Scaling of a two-layer isentropic approximation of the troposphere obtained from radiosonde data during a low-level jet event on 10–11 Dec 1977 in Brownsville, Texas (United States). Variables labeled "1" refer to the upper layer, whereas those labeled with "2" refer to the bottom layer. We show in section 3 of Part II how these values are computed and to what extent they justify the scaling chosen to derive the ismodRSW model.

	H_2 (km)	H_1 (km)	θ_1^{obs} (K)	θ_2^{obs} (K)	U_1^{obs} (m s^{-1})	U_2^{obs} (m s^{-1})	η_0
Two-layer troposphere	1.92	4.2	311.0	291.8	5.7	12.4	0.48

fluid depth h and its dimensional temperature T based on the ideal gas law and hydrostatic equilibrium, such as

$$T = T_0 h \quad \text{with} \quad T_0 = gH/R, \tag{2}$$

in which g is the acceleration due to gravity ($g = 9.81$ m s^{-2}) and H the scale height of the fluid. However, the scaling used in Kent et al. (2017)—i.e., $gH = 330$ m^2 s^{-2}, or $H \approx 34$ m—is based on an unrealistic fluid depth H and leads to an unreasonable scale temperature of $T_0 \simeq 1.1$ K. This configuration is clearly not suitable for satellite data assimilation purposes and highlights the need for a different approach. In a paper by Pan and Smith (1999), an isopycnal $1\frac{1}{2}$-layer shallow-water model is used to investigate gap winds and wakes in the presence of orography. Although the purpose of the study is different from ours, the fact that the authors used a shallow-water model and based their scaling on real atmospheric observations makes this study attractive and interesting. Remarkably, despite the use of an isopycnal model, they employed the *isentropic* definition of the reduced gravity g', that is,

$$g' = \frac{\theta_1 - \theta_2}{\theta_1} g, \tag{3}$$

to compute the Froude number utilized in their numerical simulations. On the one hand, this combined use of an isopycnal model with the isentropic definition of the reduced gravity seems to guarantee a simple but realistic testbed for their numerical experiments. On the other hand, the choice of combining together two models with two different underlying physical assumptions (i.e., constant density and constant potential temperature) cannot be seen as entirely compatible. It is precisely to remove this inconsistency that we decided to develop an entirely consistent $1\frac{1}{2}$-layer isentropic model. The ismodRSW model does not suffer from the scaling issues discussed above, and it is naturally equipped with a physically consistent temperature definition in terms of the potential temperature of each layer via Eq. (1).

The scaling of the ismodRSW model used in this paper is discussed extensively in Part II, as it is inherently linked to its analytical derivation as a reduced two-layer model. Here it suffices to say that the scenario presented in this article is based on radiosonde data during a low-level jet (LLJ) event and therefore representative of real atmospheric conditions. The values of the scale variables used in this study are summarized in Table 1.

On a further note, the transition from a single to a $1\frac{1}{2}$-layer model offers additional benefits for the modeling of idealized satellite observations. Real satellite observations are radiance measurements shaped by several processes (emission, absorption,

and scattering) taking place throughout the atmosphere before the radiance reaches the satellite. In this sense, the degree of vertical complexity with which the atmosphere can be modeled plays a crucial role in mimicking the most relevant features of real satellite observations.

b. $1\frac{1}{2}$-layer isentropic shallow water

In Part II we derive an asymptotically consistent $1\frac{1}{2}$-layer shallow-water model in which an isentropic shallow layer of fluid at potential temperature θ_2 lies below a second (relatively) motionless layer at θ_1 ($\theta_1 > \theta_2$), the latter capped by a rigid lid. This model can be considered as a reduction to $1\frac{1}{2}$-layer of the "dry" isentropic shallow two-layer model already discussed in Zeitlin (2018), although a change in the set of prognostic variables requires some attention. A sketch is given in Fig. 1. The nondimensional closed set of equations for such a system reads

$$\partial_t \sigma_2 + \mathbf{\nabla} \cdot (\sigma_2 \mathbf{v}_2) = 0, \tag{4a}$$

$$\partial_t \mathbf{v}_2 + (\mathbf{v}_2 \cdot \mathbf{\nabla}) \mathbf{v}_2 + f \mathbf{v}_2^\perp = -\mathbf{\nabla} M_2, \tag{4b}$$

$$M_1 = 0 \quad \text{and} \quad \mathbf{v}_1 = 0, \tag{4c}$$

in which σ_2 is the pseudodensity in the bottom layer defined as

$$\sigma_2 = \frac{p_r}{g}(\eta_2 - \eta_1); \tag{5}$$

$\mathbf{v}_i = (u_i, v_i)$ represents the velocity vector in the ith layer and $\mathbf{v}_2^\perp = (-v_2, u_2)$ its perpendicular component in the lower layer;
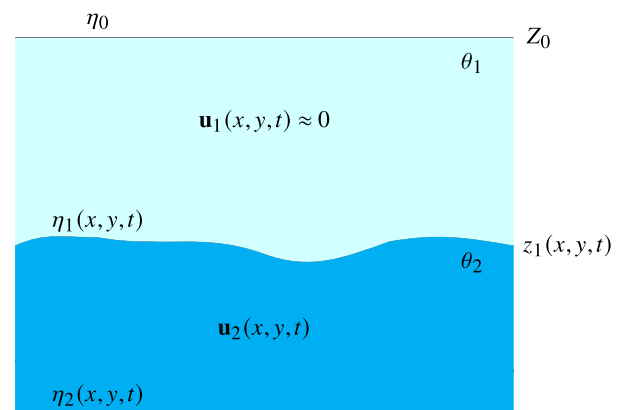

FIG. 1. Schematic representation of the $1\frac{1}{2}$-layer isentropic shallow-water model without topography ($b = 0$). Both the nondimensional pressure η_0 and the fluid depth Z_0 are constant.

f is the Coriolis frequency; M_i is the Montgomery potential of each layer. The Montgomery potential M_2 in (4b) is defined as

$$M_2 = c_p \, \theta_2 \, \eta_2^\kappa + gb, \tag{6}$$

with b representing the bottom topography. The depth of each layer is calculated as

$$h_1 = (c_p \theta_1 / g)(\eta_1^\kappa - \eta_0^\kappa); \tag{7a}$$

$$h_2 = (c_p \theta_2 / g)(\eta_2^\kappa - \eta_1^\kappa). \tag{7b}$$

For the purpose of this paper, we apply two simplifications to the system above: (i) we assume flat bottom conditions [i.e., $b = 0$ in (6)] and (ii) flow independence of the meridional direction (i.e., $\partial_y = 0$). Given these two assumptions, the equations for (σ_2, u_2, v_2) read as

$$\partial_t \sigma_2 + \partial_x (\sigma_2 u_2) = 0, \tag{8a}$$

$$\partial_t u_2 + u_2 \partial_x u_2 - f v_2 = -\partial_x M_2, \tag{8b}$$

$$\partial_t v_2 + u_2 \partial_x v_2 + f u_2 = 0. \tag{8c}$$

The system of Eqs. (8) is closed since the nondimensional pressure η_2 in (6) is linked to the pseudodensity σ_2 via its definition (5), with η_1 being

$$\eta_1 = \left[\frac{\theta_2}{\Delta\theta} \left(-\eta_2^\kappa + \frac{\theta_1}{\theta_2} \eta_0^\kappa + \frac{g}{c_p \theta_2} Z_0 \right) \right]^{1/\kappa}, \tag{9}$$

in which η_0 is the (constant) nondimensional pressure acting on the upper lid, $\Delta\theta = \theta_1 - \theta_2$ is the difference in potential temperature between the layers, and $Z_0 = h_1 + h_2$ represents the total depth of the fluid. The derivation of Eq. (9) is detailed in appendix A. A typical function relating σ_2 to η_2 for the scale variables reported in Table 1 is shown in Fig. 2.

c. The conservative hyperbolic system

The numerical implementation of the nonlinear hyperbolic system (8) can be facilitated when it is written in the following conservative form:

$$\partial_t \mathbf{U} + \partial_x \mathbf{F}(\mathbf{U}) + \mathbf{T}(\mathbf{U}) = 0. \tag{10}$$

To write the system (8a)–(8c) in conservative form, we start by multiplying (8b) and (8c) by σ_2. Replacing M_2 in the momentum equation with (6) and after some manipulation (after dropping the subscripts for σ, u, v and η), we obtain

$$\partial_t \sigma + \partial_x (\sigma u) = 0, \tag{11a}$$

$$\partial_t (\sigma u) + \partial_x (\sigma u^2) - f \sigma v = -c_p \, \theta_2 \, \sigma \, \partial_x (\eta^\kappa), \tag{11b}$$

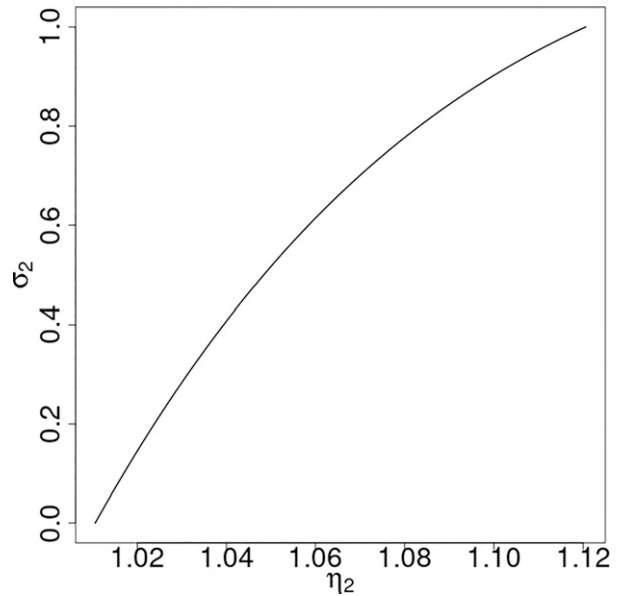$$\partial_t (\sigma v) + \partial_x (\sigma u v) + f \sigma u = 0. \tag{11c}$$

FIG. 2. Plot of nondimensional σ_2 as a function of η_2 for parameters $R = 287$ J kg^{-1} K^{-1}, $c_p = 1004$ J kg^{-1} K^{-1}, $\theta_1 = 311$ K, $\theta_2 = 291.8$ K, $\eta_0 = 0.48$, $Z_0 = 6120$ m, and $g = 9.81$ m s^{-2}.

The right-hand side of Eq. (11b) can be rewritten as the composite derivative of an unknown function $\mathcal{E}[\eta(x,t)]$:

$$-\partial_x \mathcal{E}[\eta(x,t)] = -\partial_\eta \mathcal{E} \partial_x \eta \quad \text{with} \quad \frac{\partial \mathcal{E}}{\partial \eta} = \kappa \, c_p \, \theta_2 \, \sigma(\eta) \, \eta^{\kappa-1}, \tag{12}$$

in which the analytical expression of the pseudodensity σ as a function of η reads [after substituting (9) into (5) and dropping the subscript in η_2]

$$\sigma(\eta) = \frac{p_r}{g} \left\{ \eta - \left[\frac{\theta_2}{\Delta\theta} \left(-\eta^\kappa + \frac{\theta_1}{\theta_2} \eta_0^\kappa + \frac{g}{c_p \theta_2} Z_0 \right) \right]^{1/\kappa} \right\}. \tag{13}$$

Integration of (12) with (13) yields

$$\mathcal{E}(\eta) = c_p \theta_2 \frac{p_r}{g} \frac{\kappa}{\kappa+1} \left[\eta^{\kappa+1} + \left(\frac{\theta_2}{\Delta\theta} \right)^{1/\kappa} \left(\frac{\theta_1}{\theta_2} \eta_0^\kappa \right. \right.$$
$$\left. \left. + \frac{g}{c_p \theta_2} Z_0 - \eta^\kappa \right)^{(\kappa+1)/\kappa} - \left(\frac{\theta_2}{\Delta\theta} \right)^{1/\kappa} \left(\frac{\theta_1}{\theta_2} \eta_0^\kappa + \frac{g}{c_p \theta_2} Z_0 \right)^{(\kappa+1)/\kappa} \right]. \tag{14}$$

The expression above is equivalent to the effective pressure term $P(h) = gh^2$ that would appear in an isopycnal shallow-water model and will play a crucial role in the generation of convection in the "moist" model (cf. section 4). Finally, the momentum equation can be expressed as

$$\partial_t (\sigma u) + \partial_x (\sigma u^2 + \mathcal{E}) - f \sigma v = 0, \tag{15}$$

and system (11) can be written in conservative form (10) with $\mathbf{U}, \mathbf{E(U)}$, and $\mathbf{T(U)}$ defined as follows:

$$\mathbf{U} = \begin{pmatrix} \sigma \\ \sigma u \\ \sigma v \end{pmatrix}, \quad \mathbf{F(U)} = \begin{pmatrix} \sigma u \\ \sigma u^2 + \mathcal{E} \\ \sigma u v \end{pmatrix}, \quad \mathbf{T(U)} = \begin{pmatrix} 0 \\ -f\sigma v \\ f\sigma u \end{pmatrix}. \quad (16)$$

By writing $\sigma u^2 = (\sigma u)^2/\sigma$ and $\sigma u v = (\sigma u)(\sigma v)/\sigma$, the Jacobian of the system reads as

$$\mathbf{J(U)} \equiv \partial_\mathbf{U}\mathbf{F} = \begin{pmatrix} 0 & 1 & 0 \\ -u^2 + \partial_\sigma\mathcal{E} & 2u & 0 \\ -uv & v & u \end{pmatrix}, \quad (17)$$

with eigenvalues

$$\lambda_{1,2} = u \pm \sqrt{\partial_\sigma\mathcal{E}} \quad \text{and} \quad \lambda_3 = u. \quad (18)$$

Here, $\partial_\sigma\mathcal{E}$ is computed to be

$$\frac{\partial}{\partial\eta}\mathcal{E}[\sigma(\eta)] = \frac{\partial\mathcal{E}}{\partial\sigma}\frac{d\sigma}{d\eta} \Rightarrow \frac{\partial\mathcal{E}}{\partial\sigma} = \frac{\dfrac{\partial\mathcal{E}}{\partial\eta}}{\dfrac{d\sigma}{d\eta}} = \frac{\kappa c_p \theta_2 \sigma(\eta)\eta^{\kappa-1}}{\dfrac{d\sigma}{d\eta}}, \quad (19)$$

after using (12) in the numerator and with denominator:

$$\frac{d\sigma}{d\eta} = \frac{p_r}{g}\left[1 + \left(\frac{\theta_2}{\Delta\theta}\right)^{1/\kappa}\left(\frac{\theta_1}{\theta_2}\eta_0^\kappa + \frac{g}{c_p\theta_2}Z_0 - \eta^\kappa\right)^{(1-\kappa)/\kappa}\eta^{\kappa-1}\right]. \quad (20)$$

A plot of $\partial\mathcal{E}/\partial\sigma$ in Fig. 3 shows that it is positive for nonnegative values of σ, also confirming the hyperbolic character of system (11), with real and distinct eigenvalues λ in (18) for $\partial_\sigma\mathcal{E} > 0$. The numerical scheme used to integrate the model can therefore be chosen to be close to the one in Kent et al. (2017) with minor adaptations. More details can be found in the appendix B.

3. Shrira's solution for nonlinear waves

In this section we provide an independent analytical verification of the numerical model using an extended version of Shrira's analysis of stationary nonlinear waves propagating on the surface of a rotating fluid (Shrira 1981, 1986). This verification figures as a preliminary step before extending the model to include convection and rain for future DA experiments. While a similar numerical investigation for an isopycnal single-layer shallow-water models has been conducted before (see, e.g., Bouchut et al. 2004), here we derive the analytical solution for our isentropic $1\tfrac{1}{2}$-layer configuration, with its more complicated (Montgomery) potential.

We start by splitting the pseudodensity σ into a state σ_0 and a perturbation $\tilde{\sigma}$:

$$\sigma = \sigma_0 + \tilde{\sigma} \quad \text{with} \quad \tilde{\sigma} = \frac{\sigma_0}{f}\frac{\partial v}{\partial x}. \quad (21)$$

The validity of (21) for $\tilde{\sigma}$ follows by substituting into the continuity Eq. (11a) and using the meridional momentum equation, obtaining the identity
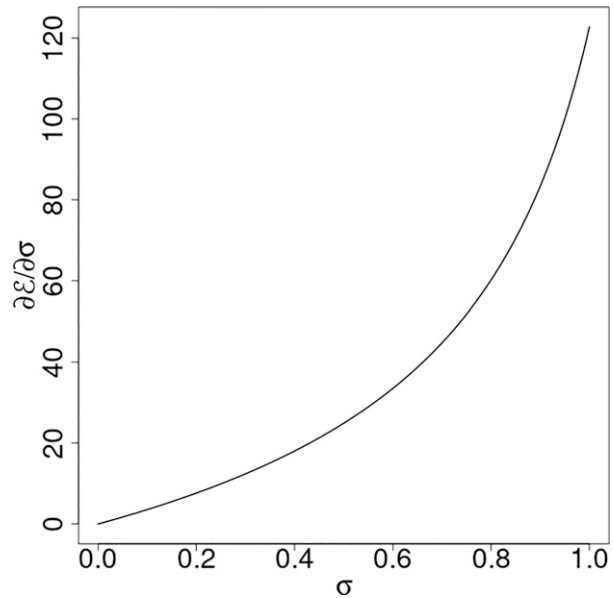

FIG. 3. Plot of nondimensional $\partial_\sigma\mathcal{E}$ as a function of σ for $R = 287$ J kg^{-1} K^{-1}, $c_p = 1004$ J kg^{-1} K^{-1}, $\theta_1 = 311$ K, $\theta_2 = 291.8$ K, $\eta_0 = 0.48$, $Z_0 = 6120$ m, and $g = 9.81$ m s^{-2}.

$$\frac{\sigma_0}{f}\frac{\partial^2 v}{\partial x\partial t} + \frac{\partial}{\partial x}\left[\left(\sigma_0 + \frac{\sigma_0}{f}\frac{\partial v}{\partial x}\right)u\right] = 0,$$

$$\frac{\partial}{\partial x}\left(\frac{\partial v}{\partial t} + fu + u\frac{\partial v}{\partial x}\right) = 0.$$

Using (8c) to express u as a function of $\partial v/\partial x$ and $\partial v/\partial t$, one finds [assuming $\partial v/\partial x + f \neq 0$]

$$u = -\frac{\partial v}{\partial t}\bigg/\left(\frac{\partial v}{\partial x} + f\right). \quad (22)$$

Differentiating (8c) by t and using both (8b) and (22) yields

$$\frac{\partial^2 v}{\partial t^2} + f^2 v - f\frac{\partial M}{\partial x} = \frac{\partial}{\partial t}\left(\frac{\dfrac{\partial v}{\partial x}\dfrac{\partial v}{\partial t}}{f + \dfrac{\partial v}{\partial x}}\right) + \frac{f}{2}\frac{\partial}{\partial x}\left[\frac{\left(\dfrac{\partial v}{\partial t}\right)^2}{\left(f + \dfrac{\partial v}{\partial x}\right)^2}\right], \quad (23)$$

resembling Eq. (10) in Shrira (1981) and Eq. (4) in Shrira (1986) (once y derivatives are dropped in the older paper and the high-frequency dispersion term is neglected).

The gradient of the Montgomery potential becomes

$$\frac{\partial}{\partial x}M[\eta(\sigma)] = \frac{\partial M}{\partial\eta}\frac{d\eta}{d\sigma}\frac{\partial\sigma}{\partial x} = c_p\theta\kappa\eta^{\kappa-1}\left(\frac{1}{\dfrac{d\sigma}{d\eta}}\right)\frac{\sigma_0}{f}\frac{\partial^2 v}{\partial x^2}, \quad (24)$$

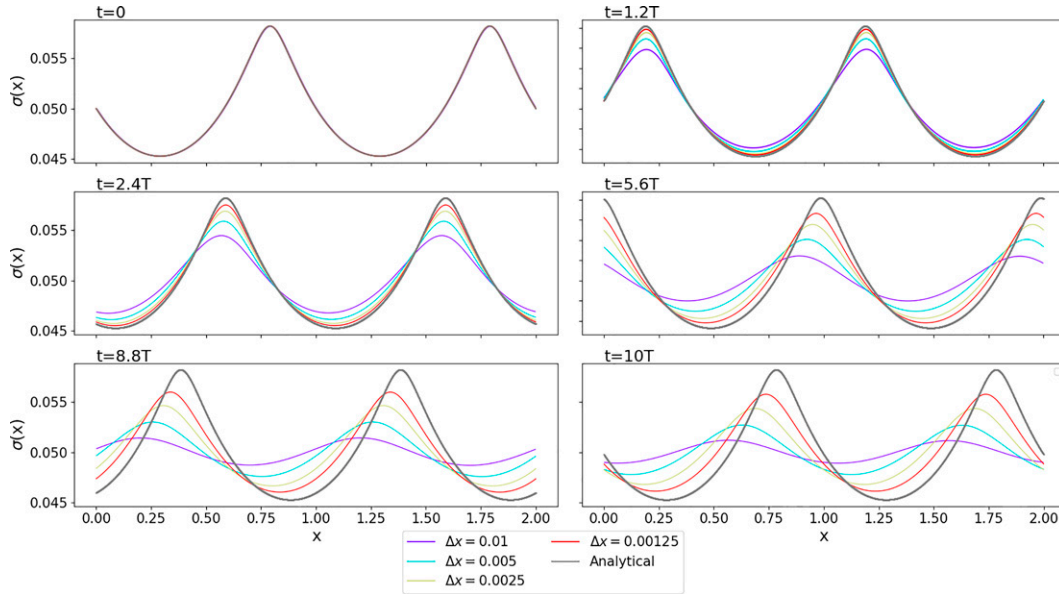after using σ' from (21). Substituting (24) into (23) gives

FIG. 4. Comparison between Shira's analytical solution for σ translated in time (gray solid line) and the evolution of the model in (11) at various spatial resolutions initialized with the same solution. Snapshots after $\{0, 1.2, 2.4, 5.6, 8.8, 10\}$ periods (T) are shown. The initial conditions are $v_0 \equiv v(x, 0) = 0.08$, $\chi_0 = 0$. The phase velocity of the wave is $c = 23.05$. Other parameters are: $\sigma_0 = 0.05$, Ro $= 0.2305$, $c_p = 1004$ J kg^{-1} K^{-1}, $\theta_1 = 311$ K, $\theta_2 = 291.8$ K, $\eta_0 = 0.48$, $p_r = 1000$ hPa, $Z_0 = 6120$ m, and CFL $= 0.5$.

$$\frac{\partial^2 v}{\partial t^2} + f^2 v - f c_p \theta \kappa \eta^{\kappa-1} \left(\frac{1}{\frac{d\sigma}{d\eta}}\right) \frac{\sigma_0}{f} \frac{\partial^2 v}{\partial x^2} = \frac{\partial}{\partial t} \left(\frac{\frac{\partial v}{\partial x} \frac{\partial v}{\partial t}}{f + \frac{\partial v}{\partial x}}\right)$$

$$+ \frac{f}{2} \frac{\partial}{\partial x} \left[\frac{\left(\frac{\partial v}{\partial t}\right)^2}{\left(f + \frac{\partial v}{\partial x}\right)^2}\right].$$

For traveling waves of phase velocity c, we define $\zeta = x - ct$ and rewrite the equation above, with primes denoting $\partial/\partial\zeta$, to obtain a second-order ODE in ζ:

$$c^2 v'' + f^2 v - f c_p \theta \kappa \eta^{\kappa-1} \left(\frac{1}{\frac{d\sigma}{d\eta}}\right) \frac{\sigma_0}{f} v'' = c^2 \left[\frac{(v')^2}{f + v'}\right]'$$

$$+ \frac{f c^2}{2} \left[\frac{(v')^2}{(f + v')^2}\right]'. \tag{25}$$

After some manipulation, one finds

$$v'' = \frac{\frac{f^2}{c^2} v}{\frac{f}{c^2} c_p \theta \kappa \eta^{\kappa-1} \left(\frac{1}{\frac{d\sigma}{d\eta}}\right) \frac{\sigma_0}{f} - \frac{f^3}{(f + v')^3}},$$

nondimensionalized as follows:

$$v'' = \frac{1}{\text{Ro}^2} \frac{v}{\frac{c_p \theta}{c^2} \kappa \eta^{\kappa-1} \left(\frac{1}{\frac{d\sigma}{d\eta}}\right) \sigma_0 - \frac{1}{\text{Ro}^3} \frac{1}{\left(\frac{1}{\text{Ro}} + v'\right)^3}}, \tag{26}$$

using $v = cv$, Ro $= c/fL$ and $(\cdot)' = \partial/\partial\zeta = (1/L)\partial/\partial\zeta' = 1/L(\cdot)'$. This ODE is solved with a Runge–Kutta fourth-order method after rewriting it as follows:

$$\chi = v', \quad \chi' = F(\chi, v, \zeta)$$

$$= \frac{\frac{1}{\text{Ro}^2} v}{\left[-\frac{1}{\text{Ro}^3} \frac{1}{\left(\frac{1}{\text{Ro}} + \chi\right)^3} + \widetilde{c_p} \theta \kappa \eta^{\kappa-1} \left(\frac{1}{\frac{d\sigma}{d\eta}}\right) \sigma_0\right]}, \tag{27}$$

with $\widetilde{c_p} = c_p/c^2$. For comparison with the full model (11), we derive the expressions also for the (nondimensional) u and $\overline{\sigma}$, using (22) and (21), and scaling u and σ_0 by c and g/p_r, respectively:

$$u = \chi/(1/\text{Ro} + \chi) \quad \text{and} \quad \overline{\sigma} = \sigma_0(1 + \text{Ro}\chi). \tag{28}$$

The solution of (27) is stable only within a certain range of initial conditions for v_0 and χ_0. Once a stable configuration is found, the phase velocity c is tuned in order to obtain a single-wavelength wave in v, u, and $\overline{\sigma}$ as solution and subsequently used as initial condition for the isentropic $1\frac{1}{2}$-layer model. A comparison between Shira's solution and its numerical implementation at various times t and up to $t = 10T$ periods is shown in Fig. 4. Although the dissipative character of the

numerical scheme used in this paper contributes to both an amplitude and a phase error as time goes by, the numerical solution (purple to red solid lines) visually converges toward the analytical one (gray line) as the resolution increases.

4. Isentropic modified 1½-layer model (ismodRSW)

a. Adding convection and rain

In this section, we extend the "dry" rotating isentropic 1½-layer model described so far to include convection and precipitation. To this end, we adopt the system of switches already used in the modRSW model (Kent et al. 2017; Kent 2016). Hence, starting from the dry model (11), a system of pseudodensity thresholds for convection (σ_c) and rain (σ_r) is introduced, in addition to an equation for the (dimensionless) rain mass fraction r, as follows:

$$\partial_t \sigma + \partial_x(\sigma u) = 0, \tag{29a}$$

$$\partial_t(\sigma u) + \partial_x(\sigma u^2 + \tilde{\mathcal{E}}) + \sigma c_0^2 \partial_x r - f\sigma v = 0, \tag{29b}$$

$$\partial_t(\sigma v) + \partial_x(\sigma u v) + f\sigma u = 0, \tag{29c}$$

$$\partial_t(\sigma r) + \partial_x(\sigma u r) + \sigma \tilde{\beta} \partial_x u + \alpha \sigma r = 0. \tag{29d}$$

The modified effective pressure $\tilde{\mathcal{E}}$ takes the value

$$\tilde{\mathcal{E}} = \begin{cases} \mathcal{E}(\sigma_c) & \text{for } \sigma > \sigma_c, \\ \mathcal{E}(\sigma) & \text{otherwise,} \end{cases} \tag{30}$$

with $\mathcal{E}(\sigma)$ defined earlier in (14); the parameter $\tilde{\beta}$ is instead equal to

$$\tilde{\beta} = \begin{cases} \beta & \text{for } \sigma > \sigma_r \text{ and } \partial_x u < 0, \\ 0 & \text{otherwise.} \end{cases} \tag{31}$$

Parameters α (s^{-1}) and β (dimensionless) control the rate at which rain is created and removed from the system. The constant speed squared c_0^2 (m^{-2} s^{-2}) converts the dimensionless rain mass fraction into a potential, introducing a coupling between the two equations and implicitly controlling the suppression of convection (see Kent et al. 2017; Kent 2016).

The mechanism described here to imitate convection and precipitation [the reader can refer to Kent et al. (2017) and Kent (2016) for more details] does not involve the implementation of a moisture equation. Instead, the thresholds σ_c and σ_r modify the dynamics of the "dry" rotating shallow-water model: convection is obtained by setting the effective pressure $\mathcal{E}$ constant whenever the pseudodensity becomes bigger than the threshold σ_c, producing a further increase in σ and therefore in the fluid depth h, akin to the rise of a buoyant air parcel. Furthermore, rain is generated whenever the pseudodensity reaches a second, higher threshold ($\sigma_r > \sigma_c$) in the presence of fluid convergence ($\partial_x u < 0$). In this model, (the word) "rain" represents the mass fraction of precipitated water: a nondimensional quantity bounded between 0 and 1. The generation and removal of rain does not alter the conservation of mass in the system and can be seen as a transfer

from and to the mass fraction of precipitable water, i.e., $1 - r$. One of the advantages of this approach is that the model can generate and remove precipitation from the system without having to be reinitialized or restarted and without having to deal explicitly with vaporization.

Similarly to the modRSW model, the ismodRSW model cannot be written in conservative form once convection and rain are added. Its intrinsic nonconservative vector formulation reads

$$\partial_t \mathbf{U} + \partial_x \mathbf{F}(\mathbf{U}) + \mathbf{G}(\mathbf{U})\partial_x \mathbf{U} + \mathbf{S}(\mathbf{U}) = 0, \tag{32}$$

where

$$\mathbf{U} = \begin{pmatrix} \sigma \\ \sigma u \\ \sigma v \\ \sigma r \end{pmatrix}, \quad \mathbf{F}(\mathbf{U}) = \begin{pmatrix} \sigma u \\ \sigma u^2 + \tilde{\mathcal{E}} \\ \sigma u v \\ \sigma u r \end{pmatrix},$$

$$\mathbf{G}(\mathbf{U}) = \begin{pmatrix} 0 & 0 & 0 & 0 \\ -c_0^2 r & 0 & 0 & c_0^2 \\ 0 & 0 & 0 & 0 \\ -\tilde{\beta} u & \tilde{\beta} & 0 & 0 \end{pmatrix}, \quad \mathbf{S}(\mathbf{U}) = \begin{pmatrix} 0 \\ -f\sigma v \\ f\sigma u \\ \alpha \sigma r \end{pmatrix}. \tag{33}$$

The Jacobian matrix $\mathbf{J} = \partial_\mathbf{U}\mathbf{F} + \mathbf{G}$ of the system is computed to be

$$\mathbf{J} = \begin{pmatrix} 0 & 1 & 0 & 0 \\ -u^2 - c_0^2 r + \partial_\sigma \tilde{\mathcal{E}} & 2u & 0 & c_0^2 \\ -uv & v & u & 0 \\ -u(\tilde{\beta} + r) & \tilde{\beta} + r & 0 & u \end{pmatrix},$$

with eigenvalues

$$\lambda_{1,2} = u \pm \sqrt{\partial_\sigma \tilde{\mathcal{E}} + c_0^2 \tilde{\beta}} \quad \text{and} \quad \lambda_{3,4} = u. \tag{34}$$

From the expression above it can be verified that this model maintains its hyperbolicity even in the presence of convection and precipitation, as the argument of the square root in (34) is nonnegative. Indeed, when only convection is activated—i.e., $\tilde{\mathcal{E}} = \mathcal{E}(\sigma_c)$ and $\tilde{\beta} = \beta = 0$—the argument of the square root takes a constant and positive value (cf. Fig. 3). Similarly, the generation of rain introduces only an additive constant given by the product of c_0^2 and β, with the latter being a nonnegative parameter by construction [cf. (31)].

The numerical scheme used for the ismodRSW model is the same as described in Kent et al. (2017) and Kent (2016), with the necessary adaptations reported in appendix B. In particular, we refer the reader to section 3.4.3 of Kent (2016) for a helpful line-by-line calculation of the nonconservative products required for the numerical implementation of the model, which takes also into account the manipulations required to handle the step functions (30) and (31). Last, given the lack of bottom topography, rotation is straightforward to implement, and it can be included as a forcing term, cf. $\mathbf{S}(\mathbf{U})$ in (32).

b. A new nature run for data assimilation

In Kent et al. (2020), we have demonstrated how the modRSW model is a viable tool to conduct data assimilation
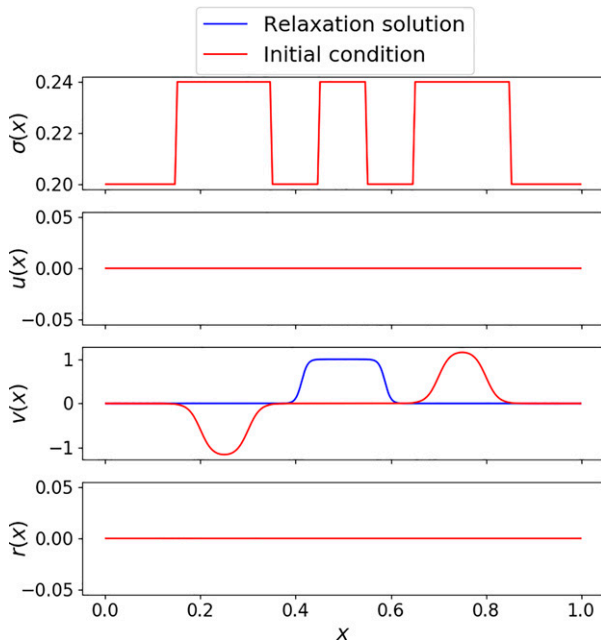
FIG. 5. Initial condition (red) and relaxation solution (blue) of the nature run simulation (parameters listed in Table 1). All variables are nondimensional.

TABLE 2. Model parameters associate to the ismodRSW nature simulation shown in Fig. 6. CFL indicates the Courant–Friedrichs–Lewy number. Please note that σ_c, σ_r, and τ_{rel} are reported as nondimensional variables. The Froude number Fr is computed as $Fr = U/\sqrt{g'H_2}$, with g' given by Eq. (3) and H_2 from Table 1.

Initial conditions	Fig. 5	η_0	0.48
Boundary conditions	Periodic	Z_0 (m)	6.12×10^3
Relaxation solution	Fig. 5	c_0^2	1.8
τ_{rel}	4	α	6.0
CFL	0.1	β	2.0
θ_1 (K)	311	σ_c	0.21
θ_2 (K)	291.8	σ_r	0.24
Ro	0.248	L (km)	500
U (m s^{-1})	12.4	N_{el}	400
T (L/U) (h)	11.2	Fr	0.36

research for operational numerical weather prediction (NWP). In particular, forecast-assimilation experiments have been conducted and subsequently analyzed to show how the system, despite its idealizations, performs akin to operational DA schemes following a variety of metrics and criteria. In Kent et al. (2020), a so-called twin-setting configuration was used, in which observations are obtained from a high-resolution deterministic run, i.e., *nature run* or simulation, whereas the background state is generated by running the model at a lower resolution. Similarly, to conduct new satellite data assimilation experiments for our novel ismodRSW model, it is essential to find a dynamically interesting nature run, characterized by continuous production of convection and precipitation. In Kent et al. (2020), the interplay between topography and a periodic domain with a zonal flow constituted a convenient setup to obtain self-generation of gravity waves. Since topography has not been developed for this model, a different configuration is needed. In this regard, it is worth bearing in mind that the numerical scheme used in this study is based on a first-order spatial discretization, which is characterized by strong numerical dissipation at low resolution, as it is evident from the evolution of the Shrira waves in Fig. 4.

To compensate for the absence of topography, we decided to introduce both rotation and a forcing term, with the latter consisting of a relaxation term in the meridional momentum equation:

$$\partial_t v + u \partial_x v + fu = (v_{rel} - v)/\tau_{rel}, \qquad (35)$$

in which τ_{rel} is a relaxation time scale defining the speed at which the meridional velocity v relaxes toward $v_{rel}(x, t)$. The relaxation profile v_{rel} is shown in Fig. 5 (blue line) and represents

a smoothed top-hat meridional jet. This type of forcing is chosen to reflect the troposphere-based scaling used in the derivation of the ismodRSW model in Part II (cf. section 4b therein), which is based on LLJ conditions: in our simplified setup, an LLJ can be approximated by a transverse jet in the meridional direction in the bottom layer of a two-layer troposphere. The initial condition used in the nature run is also shown in Fig. 5 (red lines), and represents a series of convection updraft located at the center of the domain. The shape of the initial pseudodensity profile combined with the meridional velocity produces an unstable setup that maximizes the production of convection and rain throughout the duration of the simulation. Finally, in Table 2 we list the parameter set used in the ismodRSW model to generate a 48-h-long nature run with continuous production of rain and precipitation. It is worth pointing out that the configuration described above is only a single example among a wide range of dynamical configurations that the ismodRSW model would be able to reproduce. However, here we focus on a setup that reflects the LLJ scaling conditions presented in Part II, compensates well for the numerical dissipation of our spatial discretization, and has been used in the satellite DA experiments conducted in Cantarello (2021).

The dynamical evolution of the nature run is shown in Hovmöller diagrams, one for each variable, in Fig. 6. The two top panels (right: σ; left: r) show how convection and rain are continuously generated across the (periodic) domain, as traveling waves move along it. Gray-shaded areas in the top-left panel indicate locations where only convection is activated ($\sigma_c < \sigma < \sigma_r$), whereas yellow-to-brown shadings denote areas of rain production ($\sigma > \sigma_r$). The fluid velocities are depicted in the bottom two panels (left: u; right: v). Areas of rain in the top-right panel are spatially correlated with areas where convergence in u arises, e.g., at locations where a negative gradient of u exists. The Hovmöller diagram of the meridional velocity v (bottom-right panel) shows a much smoother time evolution than the other three variables as it shows the transition from the initial condition toward the relaxation solution.

The unsettled character of the nature run is further illustrated in Fig. 7, where the time series of all variables at location $x_0 = 0.5$ are shown. The peaks and troughs in the
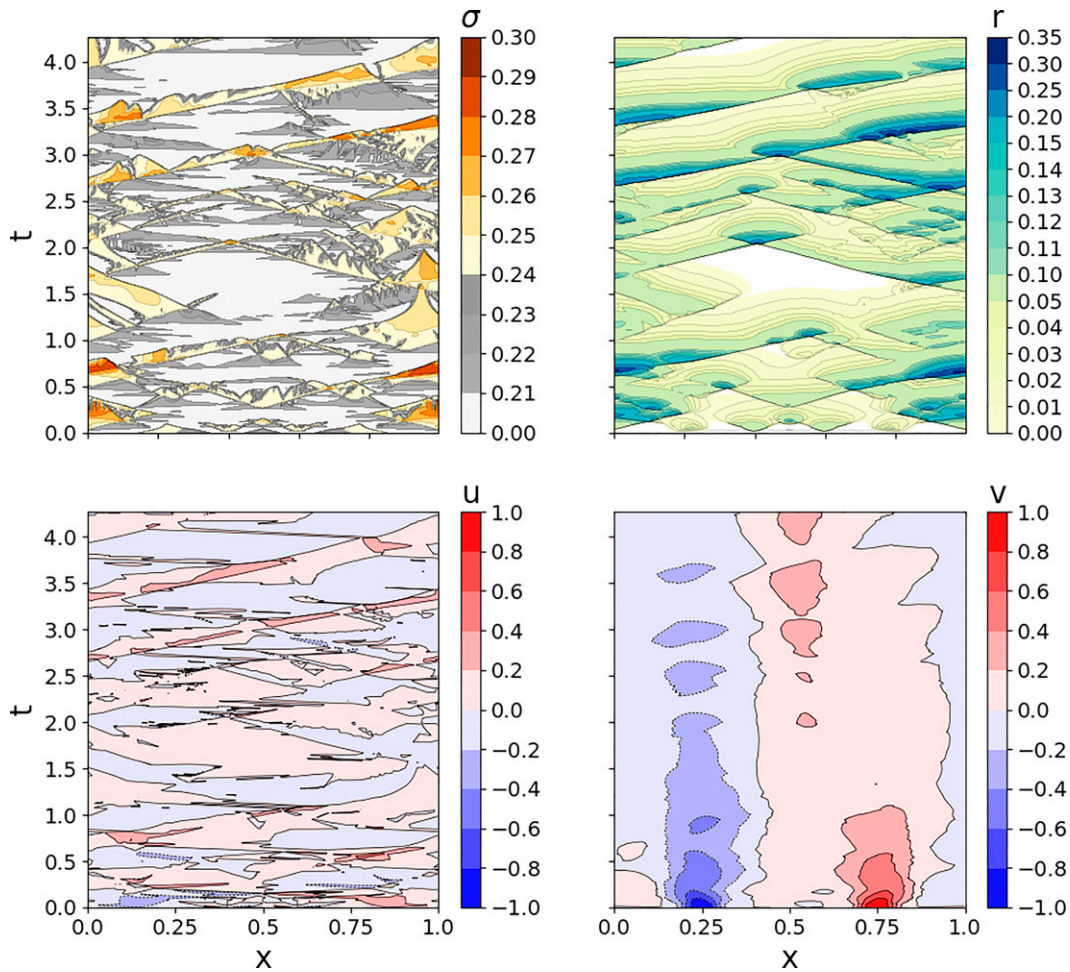
FIG. 6. Hovmöller diagrams of the nature run simulation (parameters listed in Table 2). Nondimensional variables: (top left) σ, (top right) r, (bottom left) u, and (bottom right) v. The gray and yellow shading in the top-left panel indicates the areas where σ is above the convection (e.g., $\sigma_c < \sigma < \sigma_r$) and the rain threshold ($\sigma > \sigma_r$), respectively. Note that the length of the y axis ($t = [0, 4.272]$) is the nondimensional equivalent of a 48-h period, given the scaling in Table 2.

pseudodensity $\sigma(x_0)$ indicate the passage of the gravity waves at this location, with corresponding generation and removal of rain $r(x_0)$. The transit of waves is also correlated with some irregular oscillations in the horizontal velocity $u(x_0)$, while the meridional velocity $v(x_0)$, initially zero, gradually settles toward its relaxation solution v_{rel}, that is, a jet at the center of the domain (cf. Fig. 5).

c. Recovery of the modRSW model in presence of convection and rain

As a final check performed on the full model, we want to compare the evolution in time of the modRSW against the ismodRSW model. To this end, we impose $\kappa = 1$: as we show in appendix C, this condition allows us to recover the isopycnal equations starting from the isentropic system. The two models are initialized with the same initial condition and the parameters reported in Table 2. The initial values of the fluid depth H_0, and the related thresholds H_c and H_r are scaled to

$H_0 = 1$, $H_c = \sigma_c/\sigma_0 = 1.05$, and $H_r = \sigma_r/\sigma_0 = 1.2$ with $\sigma_0 = 0.2$ (see Table 2 and Fig. 5). The value of Froude number in the bottom layer Fr_2 (which needs to be specified in the modRSW model) is reported in Table 2 and is computed as

$$\mathrm{Fr}_2 = \frac{U_2}{\sqrt{g'h_2}} = \frac{U_2}{\sqrt{g\,\dfrac{\Delta\theta}{\theta_1}\,\dfrac{R\theta_2}{g}\,\dfrac{g}{p_r}\,\sigma}}, \qquad (36)$$

in which we have used the definition of the isentropic reduced gravity g' in (3), the expression of the bottom-layer depth h_2 in (7b) and the definition of σ in (5).

We run the two models side-by-side in three different configurations: (i) classic rotating shallow water (σ_c, $\sigma_r \to \infty$), (ii) convection-only regime ($\sigma_r \to \infty$), and (iii) fully modified shallow water. The results (limited to h, σ, and r) are shown in Fig. 8. While in the first two cases (left and center panels) the two models behave identically (we notice the good agreement between the solid black for h and the dashed gray line
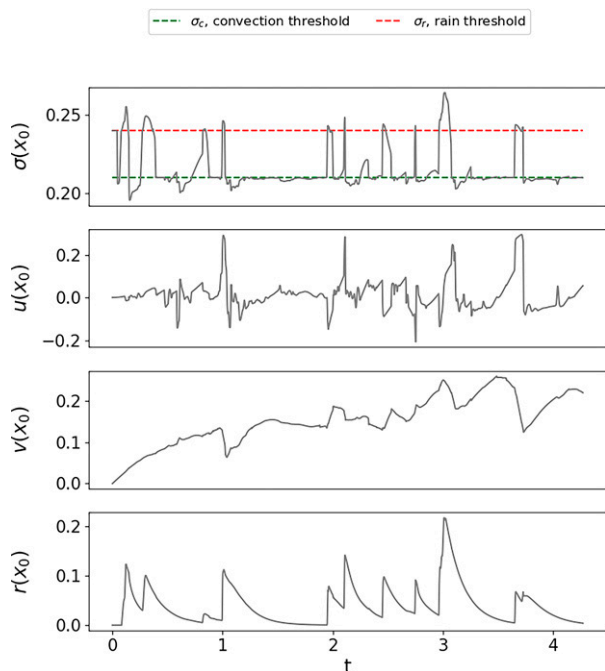
FIG. 7. Time series of the nature run variables at location $x_0 = 0.5$ (parameters listed in Table 2).

for σ in the left and center panels), we observe a gradual divergence in time between the two once both convection and rain are turned on (right panels, after $t = 0.75$). The differences are particularly noticeable in the rain solutions (blue solid and cyan dashed lines). This divergence seems to originate (and grow thereafter) at various locations in the domain where σ (and similarly h) decreases until it falls below the rain threshold. We believe this is an indirect effect of rounding errors generated by the computation of the different flux expressions in the two models [cf. Eq. (33) in this article with Eq. (6) in Kent et al. (2017)], which in turn has an impact on the values of the nonconservative products. After all, this type of behavior is not surprising given the nonlinear character of the two models.

5. Conclusions and future work

Satellite data are used extensively in data assimilation for NWP models. Their inclusion in operational systems dates back to the 1970s (Eyre et al. 2020) and represented a crucial step in a decades-long effort toward more accurate weather forecasting, with active research on how to make the best use of them continuing today. To this aim, a variety of simplified and idealized models are sometimes used, especially when the high degree of complexity and the big computational power typical of data assimilation schemes would hamper the success and the efficacy of the research on this subject.

In this paper, we presented a novel $1\frac{1}{2}$-layer isentropic model based on modified isopycnal-layer equations (ismodRSW) which has been used for satellite data assimilation research (Cantarello 2021). A companion paper (Part II) covers the

formal analytical derivation of this model without convection and precipitation.

The ismodRSW model represents an improvement of the modRSW model (Kent 2016; Kent et al. 2017) in which a single-layer of fluid at constant density is replaced by two layers at constant potential temperature capped by a rigid lid. The new model is able to mimic convection and precipitation by retaining the same mechanism based on switches already in place in the modRSW model, and initially proposed by W&C. Mimicking convection and precipitation in a shallow-water model using a system of switches represents a simpler approach than modeling moisture explicitly (as discussed, for example, in Bouchut et al. 2009; Lambaerts et al. 2011). However, the advantages are substantial: a preservation of hyperbolicity in all conditions (cf. section 4a) leading to a straightforward and robust numerical implementation, together with the possibility of generating and removing rain from the system without having to deal with vaporization explicitly. Switches are also a common feature in most state-of-the-art NWP models and therefore represent an attractive way to make idealized models more relevant for operational DA research.

The necessity for revising the modRSW model has been motivated by two of its limitations: the lack of vertical structure in the single-layer configuration and the difficulties found in defining a diagnostic relationship for temperature, cf. section 2a. Both these aspects hampered the possibility of performing meaningful satellite data assimilation experiments with the modRSW model. Our new ismodRSW model addresses those limitations, providing both a robust temperature definition within each layer and a multilayer dynamics restricted to a $1\frac{1}{2}$-layer configuration.

In this paper we provide two checks on the numerical implementation of our new model: on the one hand, we have successfully compared the numerical model (without convection and precipitation) against an analytical solution for stationary waves adapted from Shrira (1981, 1986), cf. section 3. Moreover, we demonstrated that the isopycnal model can be recovered from the isentropic for $\kappa = R/c_p = 1$. This was verified numerically by running the old and the new model side-by-side for the same physical scaling, boundary, and initial conditions. Results were identical except in the presence of both convection and rain, where small rounding errors eventually led to divergence of the two model trajectories, implicitly confirming the high nonlinearity of the system with its switches (see section 4c).

The ismodRSW model has been used to conduct idealized satellite data assimilation experiments with an ensemble Kalman filter in a twin setting configuration [cf. section 6.1 of Kent (2016), Kent et al. (2020), and Cantarello (2021)]. The model is run at two different resolutions with the observations derived from a deterministic high-resolution simulation (constituting the "truth" model trajectory, or nature run), and the low-resolution simulations treated as the forecasts. In this regard, we showed in section 4 that continuous creation and propagation of gravity waves (essential to recreate an interesting model dynamics) can be achieved with the ismodRSW model by exploiting rotation and relaxation to a given v_{rel}
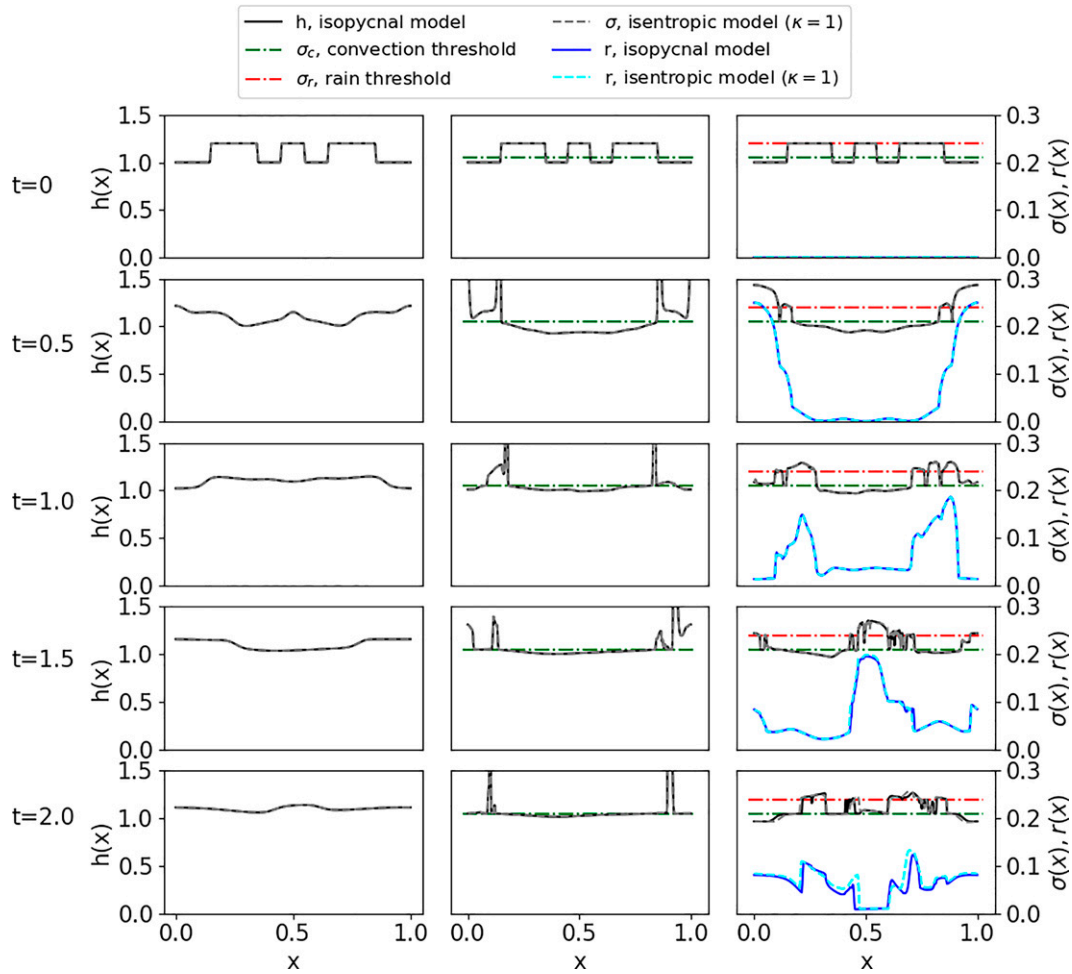
FIG. 8. Comparison between the isopycnal and the isentropic model with $\kappa = 1$ at times (from top to bottom) $t = \{0, 0.5, 1.0, 1.5, 2.0\}$. (left) Classic rotating shallow water with $\sigma_c, \sigma_r, H_c, H_r \to \infty$; (center) convection-only regime with $\sigma_c = 0.21, H_c = 1.05$ (green dashed–dotted line), and $\sigma_r, H_r \to \infty$; (right) fully modified shallow water with $\sigma_c = 0.21$, $H_c = 1.05$ and $\sigma_r = 0.24, H_r = 1.2$ (dashed–dotted red line). Variables: isopycnal fluid depth h (black solid line) and mass rain fraction r (blue solid line), isentropic pseudodensity σ (dashed gray line), and mass rain fraction r (cyan dashed line).

solution in a periodic domain, in a way that is compatible with the physical scaling based on LLJ conditions discussed in Part II, and eventually paving the way for the new forecast-assimilation experiments relevant for satellite data assimilation research described in Cantarello (2021). Another (although unexplored) option would be to exploit the analytical Shrira's solution discussed earlier which could have the potential to trigger traveling gravity waves with generation of convection and rain; even in that case, a relaxation solution can be considered to compensate for the dissipation given by the numerical scheme.

In particular, the focus of future research will be on investigating the role of satellite observations at different spatial scales, understanding what has a greater impact: whether focusing on the large-synoptic scale or, rather, the convective small-scale features. Herein, the development of a new, nonlinear observation operator [with respect to the linear one

used in Kent et al. (2020)] will be crucial. The new model will be particularly helpful, since pseudo-observations of radiance can be simulated with the help of a radiative scheme, now that a well-defined and more realistic relationship between one of the prognostic variables (in this case σ) and the layer temperature exists. Moreover, although two layers are not enough to replicate satellite weighting functions, they can be used to produce vertically integrated pseudo-observations, with weighted contributions from each layer, depending on their temperature and other (layer-dependent) radiative properties. The possibility of modeling clouds can also be taken into account by making the observation operator more elaborate: for example, convection and the rain thresholds can be used to define "nonprecipitating" and "precipitating" clouds.

Data availability statement. The observational data reported in Table 1 are derived from radiosonde data obtained from the University of Wyoming's atmospheric soundings web page (see http://weather.uwyo.edu/upperair/sounding.html).

APPENDIX A

Derivation of the Expression for η_1

In this appendix we show how to derive the expression for the dimensionless pressure η_1 in Eq. (9). The starting point is represented by Eq. (23) in Bokhove and Oliver (2009), which in the case of a two-layer model reads (i.e., $N = 2$, $\alpha = \beta = 1$)

$$M_1 = M_2 + c_p \Delta\theta \eta_1^\kappa. \tag{A1}$$

As suggested in the same paper, a constant of integration $c = -(c_p \theta_1 \eta_0^\kappa + gZ_0)$ can be added to the equation above when imposing a rigid-lid boundary condition (leading to a $1\frac{1}{2}$-layer model):

$$M_1 = M_2 + c_p \Delta\theta \eta_1^\kappa - (c_p \theta_1 \eta_0^\kappa + gZ_0). \tag{A2}$$

Substituting (6) in the above expression gives

$$M_1 = c_p \theta_2 \eta_2^\kappa + gb + c_p \Delta\theta \eta_1^\kappa - (c_p \theta_1 \eta_0^\kappa + gZ_0). \tag{A3}$$

The expression for η_1 is therefore obtained by imposing $M_1 = 0$ in (A3) in virtue of (4c) and by rearranging it appropriately (with $b = 0$ in the case of flat topography).

APPENDIX B

Numerical Scheme for the ismodRSW Model

In this appendix we summarize the numerical methods utilized to integrate the ismodRSW model. Despite some modifications, the scheme has remained the same used in Kent (2016) and Kent et al. (2017), which we refer the reader to for a more comprehensive and satisfactory description.

a. Classic shallow water

To integrate numerically the model in absence of convection and rain (i.e., the $1\frac{1}{2}$-layer isentropic shallow-water model illustrated in sections 2 and 3), a zero-degree discretization of the discontinuous Galerkin finite element method (DGFEM) developed by Rhebergen et al. (2008) is used, in combination with HLL fluxes (Harten et al. 1983). As we saw in section 2c, the shallow-water model is hyperbolic and can be put in conservative form.

We split the horizontal domain $[0, L]$ into N open elements $K_k = (x_k, x_{k+1})$ of constant length $|K_k| = x_{k+1} - x_k$ with $k = 1, 2, \ldots, N_{el}$, delimited by $N_{el} + 1$ nodes where $0 = x_1, x_2, \ldots, x_N, x_{N_{el}+1} = L$. Therefore, we derive the weak formulation of Eq. (10) [see section 3.1.2 of Kent (2016) and more extensively Zienkiewicz et al. (2014)]. The zero-degree discretization (henceforth DG-0) implies that the function $\mathbf{U}$ in (10) is approximated with a piecewise constant function within each element K_k such as

$$\mathbf{U}_h(x, t) = \overline{U}_k = \frac{1}{|K_k|} \int_{K_k} \mathbf{U}(x, t)\, dx. \tag{B1}$$

In the end, the DG-0 discretization for each element $|K_k|$ reads

$$\frac{d\overline{U}_k}{dt} + \frac{\mathcal{F}_{k+1} - \mathcal{F}_k}{|K_k|} + T(\overline{U}_k) = 0, \tag{B2}$$

where $\mathcal{F}_k$ represents the numerical flux computed at each element's node, which for the HLL fluxes is defined as

$$\mathcal{F}_k = \begin{cases} F^L & \text{if } S^L > 0, \\ F^R & \text{if } S^R < 0, \\ F^{HLL} & \text{if } S^L < 0 < S^R, \end{cases} \tag{B3}$$

with F^{HLL} defined as

$$F_i^{HLL} = \frac{F_i^L S^R - F_i^R S^L + S^L S^R (U_i^R - U_i^L)}{S^R - S^L}, \tag{B4}$$

in which S^L and S^R are the numerical velocities arising from the eigenvalues in Eq. (18):

$$S^L = \min\left(u_k - \sqrt{\partial_\sigma \mathcal{M}_k},\, u_{k+1} - \sqrt{\partial_\sigma \mathcal{M}_{k+1}}\right); \tag{B5a}$$

$$S^R = \max\left(u_k + \sqrt{\partial_\sigma \mathcal{M}_k},\, u_{k+1} + \sqrt{\partial_\sigma \mathcal{M}_{k+1}}\right). \tag{B5b}$$

It is worth noticing that in order to compute the fluxes $\mathcal{F}$ and the numerical velocities S^L, S^R, the nondimensional pressure η needs to be calculated at each time step from the pseudodensity σ. However, since inverting analytically Eq. (5) is not possible, an alternative which is efficient enough needs to be found. Here we chose to precompute the corresponding values of σ and η (with a resolution of $\delta\sigma = 0.0001$) and to perform a linear interpolation during the model integration. A polynomial interpolation is also possible.

We refer to Kent (2016) for the (adaptive) time step implementation.

b. NCPs for the full model

We noted in section 4 that the model in its full form—comprising convection and rain—cannot be put in conservative form, and that nonconservative products arise and need to be handled numerically [see Eq. (32)]. To this aim, notwithstanding the DGFEM method outlined above, the

DLM theory introduced by Dal Maso et al. (1995) is used. More details about the mathematical formulation of this scheme can be found in Kent (2016), Kent et al. (2017), and Kent and Bokhove (2020), although in this case (because of the missing topography term) there is no need to apply the state reconstruction and the well-balanced scheme developed by Audusse et al. (2004).

The following semidiscrete space-DGFEM scheme for a single element K_k is found:

$$\frac{d\overline{U}_k}{dt} + \frac{\mathcal{P}_{k+1}^p - \mathcal{P}_k^m}{|K_k|} + S(\overline{U}_k) = 0, \qquad (B6)$$

in which the numerical fluxes $\mathcal{P}_i^p$ and $\mathcal{P}_i^m$ read as

$$\mathcal{P}_i^p = \mathcal{P}_i^{\mathrm{NC}} + \frac{1}{2}\int_0^1 G_{ij}(\phi)\frac{\partial \phi_j}{\partial \tau}\,d\tau, \qquad (B7)$$

$$\mathcal{P}_i^m = \mathcal{P}_i^{\mathrm{NC}} - \frac{1}{2}\int_0^1 G_{ij}(\phi)\frac{\partial \phi_j}{\partial \tau}\,d\tau. \qquad (B8)$$

In the expressions above, $G_{ij}(\phi)$ indicates the $\{i, j\}$ matrix element of the NCP **G** matrix of Eq. (33), with ϕ being a Lipschitz continuous path connecting the left and the right state: $\phi(\tau; \mathbf{U}^L, \mathbf{U}^R) = \mathbf{U}^L + \tau(\mathbf{U}^R - \mathbf{U}^L)$, as per the DLM theory. Moreover, the NCP flux contributions $\mathcal{P}_i^{\mathrm{NC}}$ read as

$$\mathcal{P}_i^{\mathrm{NC}}(\overline{U}_i^L, \overline{U}_i^R) = \begin{cases} F_i^L - \dfrac{1}{2}\,V_i^{\mathrm{NC}}, & \text{if } S^L > 0; \\[2mm] F_i^{\mathrm{HLL}} - \dfrac{1}{2}\,\dfrac{S^L + S^R}{S^R - S^L}\,V_i^{\mathrm{NC}}, & \text{if } S^L < 0 < S^R; \\[2mm] F_i^R + \dfrac{1}{2}\,V_i^{\mathrm{NC}}, & \text{if } S^R < 0; \end{cases}$$
$$(B9)$$

with the numerical velocities S^L and S^R [cf. Eq. (34)] being

$$S^L = \min\left(u^L - \sqrt{\partial_\sigma \mathcal{M}\big|^L + c_0^2 \tilde{\beta}\big|^L},\, u^R - \sqrt{\partial_\sigma \mathcal{M}\big|^R + c_0^2 \tilde{\beta}\big|^R}\right), \qquad (B10)$$

$$S^R = \max\left(u^L + \sqrt{\partial_\sigma \mathcal{M}\big|^L + c_0^2 \tilde{\beta}\big|^L},\, u^R + \sqrt{\partial_\sigma \mathcal{M}\big|^R + c_0^2 \tilde{\beta}\big|^R}\right), \qquad (B11)$$

and $\mathbf{V}^{\mathrm{NC}}$ is a vector containing the worked-out contribution of the NCP integral expressions $\int_0^1 G_{ij}(\phi)\big(\partial \phi_j / \partial \tau\big)d\tau$:

$$\mathbf{V}^{\mathrm{NC}} = \begin{bmatrix} 0 \\ -c_0^2 [[r]]\{\{\sigma\}\} \\ 0 \\ -\beta[[u]]\Theta([[u]])\big(\sigma^R I_\beta + [[\sigma]]I_{\tau\beta}\big) \end{bmatrix}, \qquad (B12)$$

where $\Theta(\cdot)$ indicates the Heaviside function, $[[\cdot]] = (\cdot)^L - (\cdot)^R$ the jump across the node, and $\{\{\cdot\}\} = 1/2[(\cdot)^L + (\cdot)^R]$ the average quantity. I_β and $I_{\tau\beta}$ are still expressed by Eqs. (C18) and (C22) as per appendix C of Kent et al. (2017),

with analogous derivation upon the redefinition of X and Y appeared in Kent (2016) as $X = \sigma^R - \sigma^L$ and $Y = \sigma^L - \sigma_r$. The derivations of the elements in $\mathbf{V}^{\mathrm{NC}}\mathbf{V}^{\mathrm{NC}}$ are also analogous to the ones performed in the same appendix, by replacing all references to z and h with σ therein.

APPENDIX C

Recovery of the Isopycnal Model

In this appendix we show how the isentropic $1\frac{1}{2}$-layer shallow-water model can be traced back to its isopycnal counterpart by taking $\kappa = 1$ in (1). Incidentally, this should help visualize the inconsistency of using the isentropic definition of the reduced gravity, (3), within an isopycnal model.

Starting from (7b) with $\kappa = 1$, a linear relation between the fluid depth h_2 and nondimensional pressure η_2 (and thus pseudodensity σ_2) is restored:

$$h_2 = \frac{c_p \theta_2}{g}(\eta_2 - \eta_1) = \frac{c_p \theta_2}{p_r}\,\sigma_2. \qquad (C1)$$

Substituting the above expression back into the continuity Eq. (8a) yields

$$\partial_t h_2 + \partial_x(h_2 u_2) = 0, \qquad (C2)$$

equivalent to the continuity equation of the isopycnal model. In addition, we observe that for $\kappa = 1$ the Montgomery potential M_2 in (8b) becomes

$$M_2 = c_p\,\theta_2\,\eta_2.$$

By using (7) for $\kappa = 1$, we obtain

$$c_p \theta_2 \eta_2 = gh_2 + gh_1\theta_2/\theta_1 + c_p\theta_2\eta_0. \qquad (C3)$$

After using the rigid-lid constraint $H = h_1 + h_2$ and substituting back into the Montgomery potential and the momentum equation, Eq. (8b), we obtain the usual momentum equation for an isopycnal fluid:

$$\partial_t u_2 + u_2\partial_x u_2 - f v_2 = -g'\partial_x h_2, \qquad (C4)$$

with reduced gravity g' defined as in (3). However, since $\kappa = 1$ implies $\theta = T(p_r/p)$, we note that

$$\frac{\theta_1 - \theta_2}{\theta_1} = \frac{T_1/p_1 - T_2/p_2}{T_1/p_1} = \frac{1/\rho_1 - 1/\rho_2}{1/\rho_1} = \frac{\rho_2 - \rho_1}{\rho_2}, \qquad (C5)$$

making use of the ideal gas law ($p = \rho RT$). In other words, the isopycnal expression of the reduced gravity is recovered for $\kappa = 1$.

REFERENCES

Audusse, E., F. Bouchut, M.-O. Bristeau, R. Klein, and B. Perthame, 2004: A fast and stable well-balanced scheme with hydrostatic reconstruction for shallow water flows. *SIAM J. Sci. Comput.*, **25**, 2050–2065, https://doi.org/10.1137/S1064827503431090.

Bannister, R. N., 2020: The ABC-DA system (v1. 4): A variational data assimilation system for convective scale assimilation research with a study of the impact of a balance constraint. *Geosci. Model Dev.*, **13**, 3789–3816, https://doi.org/10.5194/gmd-13-3789-2020.

Bokhove, O., and M. Oliver, 2009: A parcel formulation of Hamiltonian layer models. *Geophys. Astrophys. Fluid Dyn.*, **103**, 423–442, https://doi.org/10.1080/03091920903286444.

——, L. Cantarello, and S. Tobias, 2022: An idealized $1\frac{1}{2}$-layer isentropic model with convection and precipitation for satellite data assimilation research. Part II: Model derivation. *J. Atmos. Sci.*, **79**, 875–886, https://doi.org/10.1175/JAS-D-21-0023.1.

Bouchut, F., J. Le Sommer, and V. Zeitlin, 2004: Frontal geostrophic adjustment and nonlinear wave phenomena in one dimensional rotating shallow water. Part 2. High-resolution numerical simulations. *J. Fluid Mech.*, **514**, 35–63, https://doi.org/10.1017/S0022112004009991.

——, J. Lambaerts, G. Lapeyre, and V. Zeitlin, 2009: Fronts and nonlinear waves in a simplified shallow-water model of the atmosphere with moisture and convection. *Phys. Fluids*, **21**, 116604, https://doi.org/10.1063/1.3265970.

Cantarello, L., 2021: Modified shallow water models and idealised satellite data assimilation. Ph.D. thesis, School of Mathematics, University of Leeds, 230 pp., https://etheses.whiterose.ac.uk/29672/.

Dal Maso, G., P. G. Lefloch, and F. Murat, 1995: Definition and weak stability of nonconservative products. *J. Math. Pures Appl.*, **74**, 483–548.

Ehrendorfer, M., and R. M. Errico, 2008: An atmospheric model of intermediate complexity for data assimilation studies. *Quart. J. Roy. Meteor. Soc.*, **134**, 1717–1732, https://doi.org/10.1002/qj.329.

Eyre, J. R., S. J. English, and M. Forsythe, 2020: Assimilation of satellite data in numerical weather prediction. Part I: The early years. *Quart. J. Roy. Meteor. Soc.*, **146**, 49–68, https://doi.org/10.1002/qj.3654.

Geer, A. J., and Coauthors, 2017: The growing impact of satellite observations sensitive to humidity, cloud and precipitation. *Quart. J. Roy. Meteor. Soc.*, **143**, 3189–3206, https://doi.org/10.1002/qj.3172.

——, and Coauthors, 2018: All-sky satellite data assimilation at operational weather forecasting centres. *Quart. J. Roy. Meteor. Soc.*, **144**, 1191–1217, https://doi.org/10.1002/qj.3202.

Harten, A., P. D. Lax, and B. Leer, 1983: On upstream differencing and Godunov-type schemes for hyperbolic conservation laws. *SIAM Rev.*, **25**, 35–61, https://doi.org/10.1137/1025002.

Haslehner, M., T. Janjić, and G. C. Craig, 2016: Testing particle filters on simple convective-scale models. Part 2: A modified shallow-water model. *Quart. J. Roy. Meteor. Soc.*, **142**, 1628–1646, https://doi.org/10.1002/qj.2757.

Kent, T., 2016: An idealised fluid model of numerical weather prediction: Dynamics and data assimilation. Ph.D. thesis, School of Mathematics, University of Leeds, 216 pp., https://etheses.whiterose.ac.uk/17269/.

——, and O. Bokhove, 2020: Ensuring 'well-balanced' shallow water flows via a discontinuous Galerkin finite element method: Issues at lowest order. arXiv, https://arxiv.org/abs/2006.03370.

——, ——, and S. Tobias, 2017: Dynamics of an idealized fluid model for investigating convective-scale data assimilation. *Tellus*, **69A**, 1369332, https://doi.org/10.1080/16000870.2017.1369332.

——, L. Cantarello, S. Tobias, G. Inverarity, and O. Bokhove, 2020: Idealized forecast-assimilation experiments for convective-scale numerical weather prediction. EarthArXiv, https://doi.org/10.31223/X5NG6D.

Lambaerts, J., G. Lapeyre, and V. Zeitlin, 2011: Moist versus dry barotropic instability in a shallow-water model of the atmosphere with moist convection. *J. Atmos. Sci.*, **68**, 1234–1252, https://doi.org/10.1175/2011JAS3540.1.

Migliorini, S., and B. Candy, 2019: All-sky satellite data assimilation of microwave temperature sounding channels at the Met Office. *Quart. J. Roy. Meteor. Soc.*, **145**, 867–883, https://doi.org/10.1002/qj.3470.

Pan, F., and R. B. Smith, 1999: Gap winds and wakes: SAR observations and numerical simulations. *J. Atmos. Sci.*, **56**, 905–923, https://doi.org/10.1175/1520-0469(1999)056<0905:GWAWSO>2.0.CO;2.

Petrie, R. E., R. N. Bannister, and M. J. P. Cullen, 2017: The "ABC model": A non-hydrostatic toy model for use in convective-scale data assimilation investigations. *Geosci. Model Dev.*, **10**, 4419–4441, https://doi.org/10.5194/gmd-10-4419-2017.

Rabier, F., 2005: Overview of global data assimilation developments in numerical weather-prediction centres. *Quart. J. Roy. Meteor. Soc.*, **131**, 3215–3233, https://doi.org/10.1256/qj.05.129.

Rhebergen, S., O. Bokhove, and J. J. W. van der Vegt, 2008: Discontinuous Galerkin finite element methods for hyperbolic nonconservative partial differential equations. *J. Comput. Phys.*, **227**, 1887–1922, https://doi.org/10.1016/j.jcp.2007.10.007.

Rostami, M., and V. Zeitlin, 2020: Can geostrophic adjustment of baroclinic disturbances in the tropical atmosphere explain MJO events? *Quart. J. Roy. Meteor. Soc.*, **146**, 3998–4013, https://doi.org/10.1002/qj.3884.

——, and ——, 2021: Eastward-moving equatorial modons in moist-convective shallow-water models. *Geophys. Astrophys. Fluid Dyn.*, **115**, 345–367, https://doi.org/10.1080/03091929.2020.1805448.

——, and ——, 2022: Instabilities of low-latitude easterly jets in the presence of moist convection and topography and related cyclogenesis, in a simple atmospheric model. *Geophys. Astrophys. Fluid Dyn.*, https://doi.org/10.1080/03091929.2021.1959574, in press.

Ruckstuhl, Y., and T. Janjić, 2018: Parameter and state estimation with ensemble Kalman filter based algorithms for convective-scale applications. *Quart. J. Roy. Meteor. Soc.*, **144**, 826–841, https://doi.org/10.1002/qj.3257.

Rudd, A. C., I. Roulstone, and J. Eyre, 2012: A simple column model to explore anticipated problems in variational assimilation of satellite observations. *Environ. Modell. Software*, **27–28**, 23–39, https://doi.org/10.1016/j.envsoft.2011.10.001.

Shrira, V., 1981: Propagation of long nonlinear waves in a layer of rotating fluid. *Sov. Phys. Izvestija*, **17**, 55–59.

——, 1986: On the long strongly nonlinear waves in rotating ocean. *Sov. Phys. Izvestija*, **22**, 285–305.

Simmons, A. J., and A. Hollingsworth, 2002: Some aspects of the improvement in skill of numerical weather prediction. *Quart. J. Roy. Meteor. Soc.*, **128**, 647–677, https://doi.org/10.1256/003590002321042135.

Smith, P. J., A. M. Fowler, and A. S. Lawless, 2015: Exploring strategies for coupled 4D-Var data assimilation using an idealised atmosphere–ocean model. *Tellus*, **67A**, 27025, https://doi.org/10.3402/tellusa.v67.27025.

Stewart, L. M., S. L. Dance, and N. K. Nichols, 2013: Data assimilation with correlated observation errors: Experiments with a 1-D shallow water model. *Tellus*, **65A**, 19546, https://doi.org/10.3402/tellusa.v65i0.19546.

Vetra-Carvalho, S., S. Migliorini, and N. Nichols, 2011: Ensemble data assimilation in the presence of cloud. *Comput. Fluids*, **46**, 493–497, https://doi.org/10.1016/j.compfluid.2011.01.033.

Würsch, M., and G. C. Craig, 2014: A simple dynamical model of cumulus convection for data assimilation research. *Meteor. Z.*, **23**, 483–490, https://doi.org/10.1127/0941-2948/2014/0492.

Zaplotnik, Ž., N. Žagar, and N. Gustafsson, 2018: An intermediate-complexity model for four-dimensional variational data assimilation including moist processes. *Quart. J. Roy. Meteor. Soc.*, **144**, 1772–1787, https://doi.org/10.1002/qj.3338.

Zeitlin, V., 2018: *Geophysical Fluid Dynamics: Understanding (Almost) Everything with Rotating Shallow Water Models.* Oxford University Press, 488 pp.

Zeng, Y., T. Janjić, A. de Lozar, U. Blahak, H. Reich, C. Keil, and A. Seifert, 2018: Representation of model error in convective-scale data assimilation: Additive noise, relaxation methods, and combinations. *J. Adv. Model. Earth Syst.*, **10**, 2889–2911, https://doi.org/10.1029/2018MS001375.

——, ——, M. Sommer, A. de Lozar, U. Blahak, and A. Seifert, 2019: Representation of model error in convective-scale data assimilation: Additive noise based on model truncation error. *J. Adv. Model. Earth Syst.*, **11**, 752–770, https://doi.org/10.1029/2018MS001546.

Zienkiewicz, O., R. Taylor, and P. Nithiarasu, 2014: *The Finite Element Method for Fluid Dynamics.* 7th ed. Butterworth-Heinemann, 756 pp.